Fluid-particle suspension by gas release from a granular bed

Tess Homan,[1,2] Valérie Vidal,[1] Clément Picard,[1] and Sylvain Joubaud[1,3,*]
[1]Univ Lyon, ENS de Lyon, Univ Claude Bernard, CNRS, Laboratoire de Physique, Lyon, France
[2]Mechanical Engineering, Eindhoven University of Technology, Eindhoven, The Netherlands
[3]Institut Universitaire de France (IUF), 1 rue Descartes, 75005 Paris, France

(Received 1 February 2020; accepted 12 August 2020; published 16 October 2020)

We have studied experimentally particle suspension when injecting a gas at the bottom of an immersed granular layer confined in a Hele-Shaw cell. This work focuses on the dynamics of particles slightly denser than the surrounding fluid. The gas, injected at a constant flow-rate, rises through the granular bed and then forms bubbles that entrain particles in the above liquid layer. The particles settle down on the edges of the cell, avalanche on the crater formed at the granular bed free surface, and are further entrained by the continuous bubbling at the center. We report the existence of a stationary state, resulting from the competition between particle entrainment and sedimentation. The average solid fraction in the suspension is derived from a simple measurement of the granular bed apparent area. A phenomenological model based on the balance between particle lift by bubbles at the center of the cell and their settling on its sides demonstrates that most of the particles entrained by bubbles come from a global recirculation of the suspension.

DOI: 10.1103/PhysRevFluids.5.104304

I. INTRODUCTION

Recently, there has been a growing research interest in multiphase flows, as their understanding is one of the grand natural and industrial challenges in fluid dynamics [1]. Among the multitude of geophysical flows, gas release in a particle-laden fluid is a widespread phenomenon that may have drastic consequences on the environment [2]. On the one hand, the understanding of methane production and transport in sedimentary basins and its subsequent release is crucial in terms of climate change and global warming [3–5]. On the other hand, exsolved volatiles rising through crystal-rich magmas strongly influence volcanic eruption dynamics [6–8]. Quantifying the mechanisms leading to such resuspension and the generated turbidity current is also essential for the effects of human activities from the production of crude oil from the Canadian oil sands [9] and to deep-sea mining [10]. In industry, catalytic gas-fluidized bed reactors have been widely investigated for the optimization of chemical processes [11–13]. In most of these applications, the interplay between the gas and the particles is one of the key parameters of the global dynamics of such multiphase flows. Therefore, understanding and quantifying the ability of gas to entrain and maintain particles in suspension is a question of paramount importance.

To tackle this question, we consider particle entrainment from immersed granular beds. The resuspension of particles forming this solid-like settled state and the induced erosion, chimney formation, or crater formation have been investigated using different mechanisms such as shearing flow [14,15], the impact of liquid jets [16–19], thermal convection or plume emission [20–24], underground cavity collapse [25], fluidization [26], etc. The present paper focuses on gas release

*Corresponding author: sylvain.joubaud@ens-lyon.fr

TABLE I. Characteristics of the polystyrene (PS) or polyvinyl chloride (PVC) beads used in the experiments. $\Delta\rho = \rho_g - \rho_\ell$ is the density difference between the particles and the fluid, d is the typical particle diameter, and φ_b^0 is the initial bed solid fraction (see text). $U_s = \Delta\rho g d^2/(18\mu)$ is the Stokes (settling) velocity of a single particle of typical diameter d in a fluid of viscosity μ (see Sec. IV). $\mathrm{Ar} = \rho_\ell U_s d/\mu$ is the Archimedes number, which corresponds to the particle Reynolds number based on the Stokes velocity U_s.

Particles	Provider	Shape	Distribution	$\Delta\rho$ (kg/m^3)	d (μm)	φ_b^0 (%)	U_s (mm/s)	Ar
PVC 110P	Goodfellow®	nonspherical	polydisperse	590	110 ± 50	41.9 ± 0.5	3.2	0.23
PS 130P	Goodfellow®	nonspherical	polydisperse	270	130 ± 80	42.0 ± 0.5	2.1	0.18
PS 250M	Dynoseeds®	spherical	monodisperse	270	230 ± 10	56.2 ± 0.5	6.5	0.98
PS 80M	Dynoseeds®	spherical	monodisperse	270	80 ± 5	57.8 ± 0.5	0.8	0.04

from a granular bed, a scenario highlighted in the above applications. In the past years, two classes of model systems have been developed to exhibit the physical mechanisms at stake in such three-phase flows, where the coupling between the grains, gas, and liquid may have a strong impact on the global dynamics. On the one hand, to remove or neglect the effect of gravity, experiments have been performed in horizontal setups and/or using isodense particles [27–35]. On the other hand, buoyancy-driven systems have mostly focused on gas patterns in a dense granular bed, with particles much heavier than the surrounding fluid [36–43]. Depending on the gas injection flow rate or pressure and the local solid fraction, the gas may either percolate through the grains or fracture the bed. At the grain free-surface, the successive ejection of gas bubbles entrains particles in the liquid. The competition between the particle lift and sedimentation leads at long time to crater formation [39].

In the present paper, we study experimentally the global characteristics of the suspension formed by particles slightly heavier than the surrounding fluid, which are entrained by continuous gas injection. In particular, we focus on the balance between entrainment by the bubble rise and sedimentation. The goal is to identify and quantify the controlling parameters of the extension and average solid fraction of the suspension. We demonstrate that this latter can be estimated at each time from the size of the granular bed which remains at the cell bottom. We then quantify the existence and properties of a steady state when varying the cell geometry and particle properties. We finally propose a simple model based on the balance between entrainment and sedimentation, which unravels the particle entrainment mechanism in the stationary state.

The paper is organized as follows. After a description of the experimental setup (Sec. II), the analysis of the experimental results and the influence of the various parameters is presented in Sec. III. In a second stage, the different ingredients of a simple model are presented in Sec. IV, and its predictions are compared to the experimental results in Sec. V. Finally, we conclude and draw some perspectives in Sec. VI.

II. EXPERIMENTAL SETUP

The experimental setup, sketched in Fig. 1(a), consists of a vertical Hele-Shaw cell of height 30 cm, width L_c ($L_c = 13.6$, 24.0, or 35.6 cm), and gap e ($e = 2$ or 3 mm). The cell is filled with ethanol (absolute, Merck Millipore, density $\rho_\ell = 789$ kg/m^3, viscosity $\mu = 1.2 \times 10^{-3}$ Pa s) and beads of either polystyrene (PS, density $\rho_g = 1059$ kg/m^3) or polyvinyl chloride (PVC, density $\rho_g = 1379$ kg/m^3), with different sizes and shapes [typical diameter d, monodisperse (M) or polydisperse (P); see Table I]. Images of the different batches are displayed in Figs. 1(b)–1(e). Note that the use of ethanol prevents the formation of particles aggregates. Air is injected at a constant flow-rate Q at the bottom of the cell through a central gas-inlet (inner diameter 1 mm). The flow-rate is varied between $Q = 0.013$ and 1.5 L/min by means of a mass-flow controller (Bronkhorst, Mass Stream D-5111 for $0.01 \leqslant Q \leqslant 0.05$ L/min and D-6311 for $0.05 \leqslant Q \leqslant 2$ L/min). A reproducible

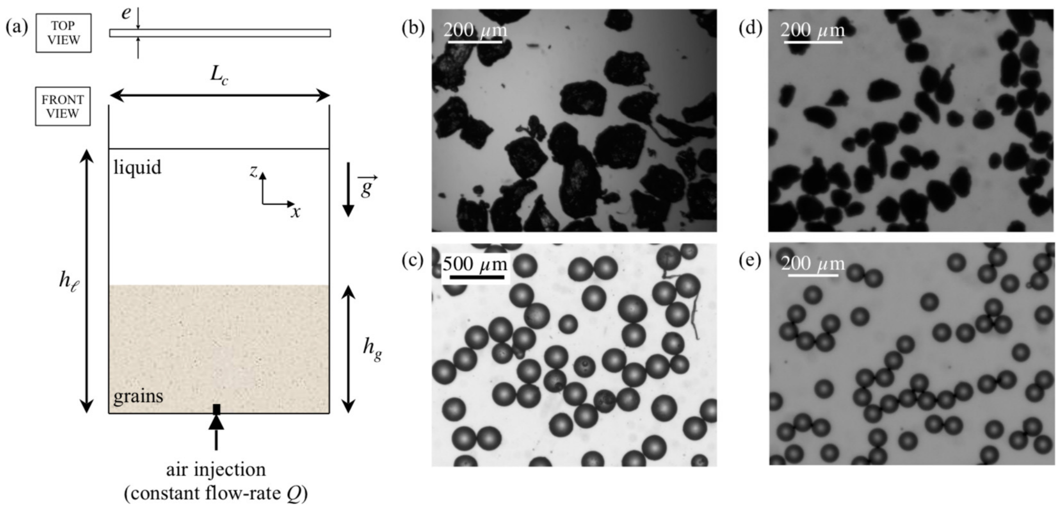

FIG. 1. (a) Schematic view of the experimental setup. Air is injected at a constant flow rate Q at the bottom of an immersed granular layer in a Hele-Shaw cell (see text). The subsequent suspension and the remaining granular bed are observed using shadowgraphy. The different notations of the geometrical parameters are indicated. On the right, images of different batches of grains (see Table I): (b) nonspherical polydisperse polystyrene beads (PS 130P); (c) spherical monodisperse polystyrene beads (PS 250M); (d) nonspherical polydisperse PVC beads (PVC 110P); (e) spherical monodisperse PS beads (PS 80M).

initial condition is obtained by mixing the particles and the liquid with a strong air flow-rate (2 L/min) for 3 min. The air flow is then turned off and the particles are left to sediment gently, leading to a homogeneous loose-packing initial bed. As expected, the obtained solid fraction, φ_b^0, for the monodisperse spherical particles corresponds to a random loosely packed state [44] (Table I). Note that φ_b^0 is much smaller for polydisperse nonspherical angular particles, for which the bed is in a very loose state [45] (Table I). The initial bed height, h_g, is varied up to 10 cm and the liquid height is adjusted to a given value $h_\ell > h_g$ [see Fig. 1(a)]. The ratio h_ℓ/h_g lies in the range 1.2–4.

The setup is illuminated from behind by a strong homogeneous backlight (Dalle LED, Euroshopled). Shadowgraph imaging of the container, the granular bed, and the suspension is performed using a camera (PixeLINK, PL-B741U) capturing images at 1 Hz. A contour detection, based on intensity thresholding, makes it possible to infer the granular bed area A, and thus its volume $A \cdot e$, for each image, and to get its temporal evolution during each experiment. We denote A_0 the initial bed area and $h_g = A_0/L_c$ as the initial bed height. Finally, bubble contour detection is performed in the suspension in the stationary regime to quantify the typical bubble size (see Sec. V A).

III. EXPERIMENTAL RESULTS

A. Phenomenology

Figure 2 displays a typical experiment, where a time-lapse shows the evolution of the granular bed and the suspended particles. At $t = 0$ s, air is injected at a constant flow rate Q at the bottom of the immersed granular bed. The gas initially invades the granular bed, then air bubbles escape and rise through the liquid layer above, entraining particles in their wake [Figs. 2(c)–2(f)]. This process leads to the formation of a crater that increases with time [Figs. 2(c)–2(f)]. When the particles deposit on the inner part of the crater, they avalanche back to the center and are further entrained by the continuous gas injection. The system finally reaches a stationary state [Figs. 2(f)–2(h)] characterized by a *suspension*, resulting from the balance between particles lifted by gas bubbles

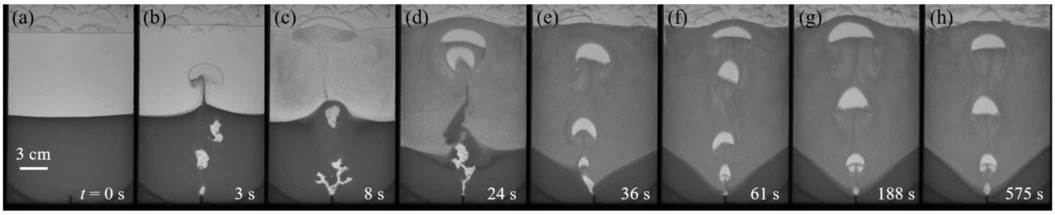

FIG. 2. Temporal evolution of the bed and suspension (PS 130P, $Q = 200$ mL/min, $h_g = 10 \pm 0.2$ cm, $h_\ell = 20 \pm 0.2$ cm, $L_c = 13.6$ cm, $e = 2$ mm). (a) Initial loosely-packed bed. (b), (c) After turning on the gas injection, air rises through the granular bed and forms bubbles that entrain particles in their wake in the above liquid layer. (d), (e) A crater grows and the suspension becomes denser. (f)–(h) The system reaches a stationary state in which the volume of the granular bed and the average solid fraction of the suspension remain constant.

and sedimentation; and a *granular bed*, corresponding to the particles that are not entrained by the gas flow. Note that a small transition region exists between the granular bed and the suspension, corresponding to the avalanching particles, slightly less dense than the granular bed. Its size is at most a few percent of the granular bed's size and is included in the bed area, A, by our thresholding method.

To carefully investigate the existence and the characteristics of this stationary state, experiments have been performed for a wide range of experimental parameters. Typical snapshots are shown in Fig. 3 for different flow rates Q and cell widths L_c. At constant L_c, when increasing Q, we observe that the area occupied by the granular bed decreases and the suspension becomes darker, confirming that its solid fraction increases. In addition, the typical width occupied by the suspension, denoted as L_s, increases until it reaches the lateral boundaries of the cell, L_c. In most of our experiments, $L_s \simeq L_c$. In this work, except when explicitly mentioned, we will focus on this configuration only.

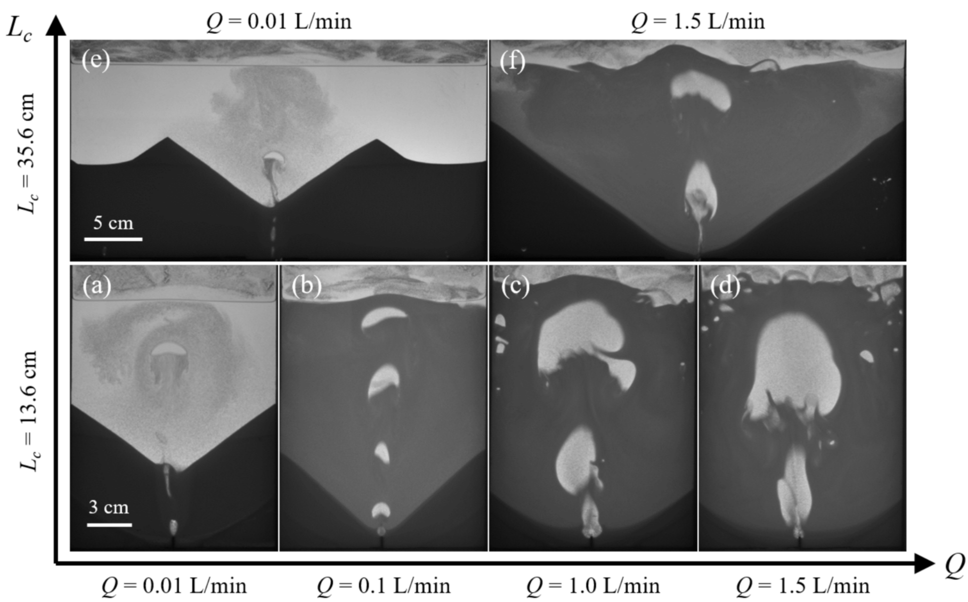

FIG. 3. Snapshots of the experiments in the stationary regime for different values of the flow rate Q and different cell width L_c (PVC 110P, $h_g = 9 \pm 0.5$ cm, $h_\ell = 18 \pm 0.5$ cm). The thickness of the cell is $e = 2$ mm for the lower panel ($L_c = 13.6$ cm) and $e = 3$ mm for the upper panel ($L_c = 35.6$ cm).

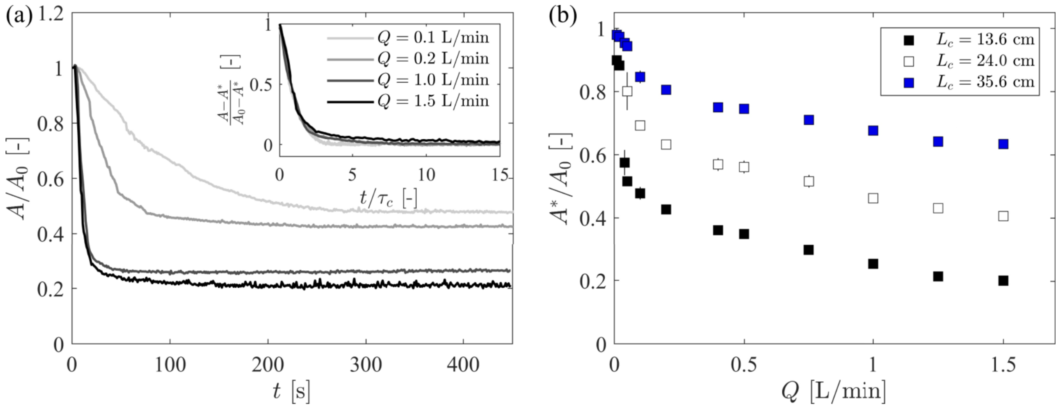

FIG. 4. (a) Temporal evolution of the normalized bed area, A/A_0, for different air flow-rate Q (decreasing from light gray to dark gray). Experimental parameters are those given in the caption of Fig. 3 (PVC 110P, $h_g = 9 \pm 0.5$ cm, $h_\ell = 18 \pm 0.5$ cm, $L_c = 13.6$ cm, $e = 2$ mm). Inset: Normalized plot, $(A - A^*)/(A - A_0)$, as a function of t/τ_c. (b) Normalized bed area in the stationary state, A^*/A_0, as a function of the injected air flow-rate Q for different cell widths ($e = 2$ mm for $L_c = 13.6$ and 24.0 cm and $e = 3$ mm for $L_c = 35.6$ cm).

While we retrieve the typical crater shape with two dunes reported by [39] for small Q and large L_c (top-left snapshot in Fig. 3), the flank of the crater is limited by the cell boundary for large Q and/or small L_c.

The crater and suspension characteristics in the stationary state do not depend on the finite width of the cell only, but also on the number and type of particles and the volume of liquid available above the granular bed. The influence of these parameters is presented in the Appendix showing typical snapshots of the stationary state when changing the granular bed height h_g, the total height of the liquid h_ℓ, and the batch of particles. It can be seen that both h_ℓ and h_g have an effect on the intensity, and therefore the solid fraction of the suspension (see Fig. 9 in the Appendix). However, no clear trend can be highlighted. Finally, as expected, the small particles (PS80 M) are more easily put into suspension than larger particles (PS 250M) (see Fig. 10 in the Appendix).

B. Temporal evolution and quantitative measurement of the granular bed size

Figure 4(a) displays the temporal evolution of the normalized bed volume (or area), A/A_0, defined as its surface A times the cell gap e, relative to the initial bed volume, A_0e. For different air injection flow rates Q (increasing from 0.1 to 1.5 L/min), the system always reaches a stationary regime in which the volume of the granular bed remains constant. The final area of the bed is denoted A^*. As expected, the characteristic time τ_c to reach the steady state for A/A_0 decreases when increasing Q. Such behavior was previously reported for the fluidization of a heavy particle bed ($d \sim 3$ mm, $\rho_g = 2230$ kg/m^3) in two-phase systems [46]. The normalized plot $(A - A^*)/(A - A_0)$ as a function of t/τ_c is displayed as an inset of Fig. 4(a) and shows that all the curves collapse on the same master curve, indicating that the dependance of τ_c on Q is related to the dependance of A^* on Q. In the present paper, we focus only on the characteristics of the granular bed and the suspension in the stationary regime. In the following, the quantities in the stationary state are denoted with an asterisk.

To quantity the phenomenological observations, the final volume of the granular bed as a function of the flow rate is displayed in Fig. 4(b) for different values of the cell width L_c. For each cell width, A^*/A_0 decreases with Q. It drops abruptly at small flow rates $Q < 250$ mL/min, while for $Q > 250$ mL/min the size of the granular bed decreases more gently. In addition, the decrease of A^*/A_0 as a function of Q is more abrupt for small cell widths. Thus, more particles remain in the granular bed when increasing the flow-rate for large L_c compared to small L_c. This result can easily be explained, since for large L_c most particles are far from the injection point and a larger flow rate

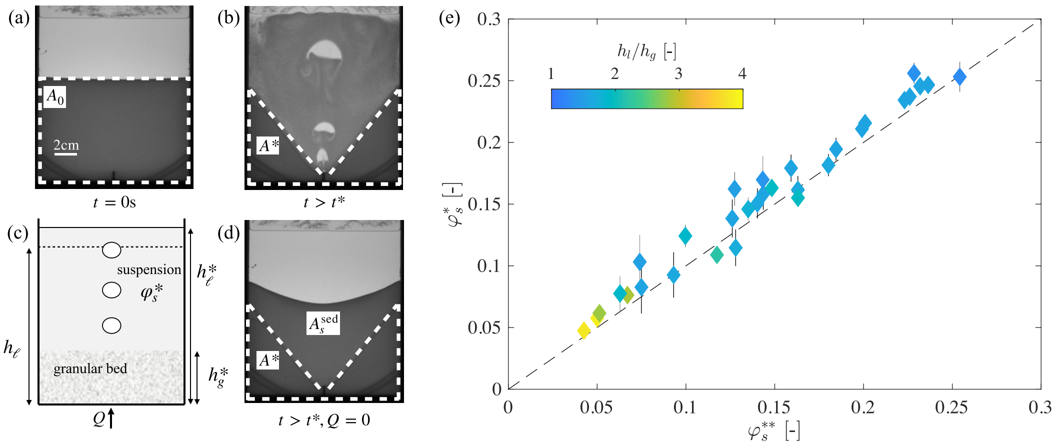

FIG. 5. Snapshots of the experiments just before turning on the flow rate (a) and in the stationary regime (b) (PS 130P; $Q = 100$ mL/min; $L_c = 13.6$ cm; $e = 2$ mm; $h_g = 9.3 \pm 0.5$ cm; $h_\ell = 14.4 \pm 0.5$ cm). (c) Schematic view of the mass conservation model used to compute the solid fraction of the suspension. (d) Snapshot of the experiment after turning off the flow rate. (e) Solid fraction of the suspension φ_s^*, computed using the mass conservation model [Eq. (3)], as a function of φ_s^{**}, computed using the number of particles that have sedimented after turning off the flow rate for different ratio h_ℓ/h_g. The error bars correspond to the estimation of the compaction of the granular bed [$\phi_b^* = (1.05 \pm 0.05)\phi_b^0$]. The dashed line corresponds to the first bisector.

is necessary to reach them. In addition, when the particles are resuspended into the fluid, they have a larger volume they can occupy for a large cell than for a small cell. The solid fraction of the induced suspension is therefore also smaller for large L_c.

C. Mean solid fraction of the suspension

As underlined in the Introduction, an important quantity is the number of particles in the particle-laden liquid above the granular bed. In the previous section, we qualitatively comment on the solid fraction of the suspension. Here, we present a quantitative method to compute the mean solid fraction φ_s^* of the suspension from the measurement of the final bed size A^*/A_0 using mass conservation. The total number of particles in the suspension, denoted N_s^*, occupies a volume $V_s^* = A_s^* e$, where A_s^* is the area occupied by the suspension. The mean solid fraction of the suspension can therefore be written as $\varphi_s^* = N_s^* V_g / V_s^*$, where $V_g \simeq (4/3)\pi(d/2)^3$ is the typical grain volume. The final bed size, A^*/A_0, and φ_s^* are not independent variables, since they are directly linked by the particle mass conservation. Indeed, the number of grains N_g is fixed in the experiment and can be computed using the bed area in the initial state [Fig. 5(a)]. In the stationary state [Fig. 5(b)], it can be decomposed into two populations: $N_{\rm bed}^*$ particles, which are still in the granular bed, and N_s^* particles, which have been lifted in suspension, such that

$$N_g = N_{\rm bed}^* + N_s^*. \tag{1}$$

Using the definition of the solid fraction, one can get

$$\varphi_b^0 A_0 = \varphi_b^* A^* + \varphi_s^* A_s^*, \tag{2}$$

where φ_b^* is the solid fraction of the granular bed in the stationary state. At the beginning of the experiment, we observe a quick compaction by a few percent of the granular bed. This observation can be related to the compaction reported classically for dry or immersed granular beds under mechanical vibrations, which are triggered here by the upward flow [47]. After this quick compaction, the bed packing remains constant. To get an estimate of the volume occupied by the suspension, a typical sketch of the stationary state regime is proposed in Fig. 5(c). The liquid height in the stationary state h_ℓ^* is larger than in the initial condition due to the presence of the bubbles. Moreover, in most of the experimental configurations presented in this paper, the suspension has reached the side boundaries of the cell. In the following, we consider only data for which $L_s \simeq L_c$. The volume occupied by the suspension is therefore equal to $h_\ell^* L_c e - A^* e - V_{\text{Bubbles}}$, where the final volume of the granular bed, $A^* e$, and the volume of the bubbles, V_{Bubbles}, have been subtracted to the total volume $h_\ell^* L_c e$ occupied by the system. Since the liquid is incompressible, $h_\ell^* L_c e - V_{\text{Bubbles}}$ is simply equal to $h_\ell L_c e$. After some algebra, one gets the solid fraction in the suspension, in the stationary regime, as a function of A^*/A_0:

$$\varphi_s^* = \frac{\varphi_b^0 - (A^*/A_0)\varphi_b^*}{(h_\ell/h_g) - (A^*/A_0)}. \tag{3}$$

This estimate can be compared to a more direct measurement of the number of particles in the suspension. At the end of the experiment, the air flow is turned off and all the particles in suspension sediment in a loose packing granular bed with the same solid fraction as the initial state, φ_b^0. Since φ_b^0 and φ_b^* are slightly different, two regions in this final granular state can be distinguished [Fig. 5(d)]: the granular bed of size A^* and the bed formed by the particles previously in the suspension of size A_s^{sed}. The solid fraction in the latter bed is equal to

$$\varphi_b^0 = \frac{N_s^* V_g}{A_s^{\text{sed}} e}. \tag{4}$$

Using Eq. (4) and the expression of the volume occupied by the suspension as a function of A^*, one can get a second estimate of the solid fraction of the suspension, denoted φ_s^{**}, as

$$\varphi_s^{**} = \frac{N_s^* V_g}{V_s^*} = \varphi_b^0 \frac{A_s^{\text{sed}}}{h_\ell L_c - A^*}. \tag{5}$$

Figure 5(e) displays the solid fraction measured in the stationary state, φ_s^*, as a function of the one computed at the end of the experiment, φ_s^{**}, for different values of the height ratio, h_ℓ/h_g. As expected, all the data points collapse on the first bisector within experimental error bars, showing that the two estimates are in very good agreement, which validates the computation of the suspension solid fraction using the final bed size. For all experiments, we can thus determine the average solid fraction in the suspension, φ_s, at all times. In the following sections, we focus on the stationary state, where the solid fraction is denoted φ_s^*.

IV. PHENOMENOLOGICAL MODEL

In this section, we propose a phenomenological model to explain the dependence of the spatial average solid fraction in the suspension, φ_s, on the experimental parameters. In the stationary state the suspension results from the balance between grains advected by the bubbles rising in the above liquid layer, and particles settling on the sides. The following subsections propose an expression of the number of particles sedimenting on the sides of the cell (Sec. IV A) or entrained by the bubbles at the center (Sec. IV B), with a final expression of the suspension average solid fraction in the stationary state, φ_s^*, resulting from the competition between both mechanisms (Sec. IV C).

A. Particle settling

Let us denote dN^+ the number of particles dV^+ of the suspension settling on the granular bed during the time interval dt [Fig. 6(a), dark gray zones on the suspension sides],

$$dN^+ = \varphi_s \frac{dV^+}{V_g} = \varphi_s \frac{(L_s - L_b) e U_p dt}{V_g}, \tag{6}$$

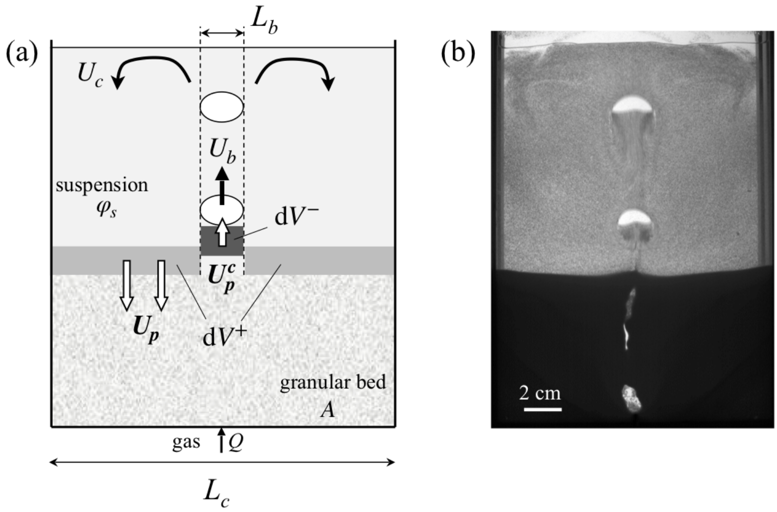

FIG. 6. (a) Sketch of the fluid-particle suspension by gas injection (phenomenological model; see Sec. IV). Gas is injected at a constant flow rate Q at the bottom center of the cell and crosses the granular bed. Bubbles rising in the above liquid layer (velocity U_b) entrain particles upward in the central column (width L_b) and form a suspension of width L_S that is of the order of L_c in all the data discussed in Sec. IV. Particles on both sides settle due to both sedimentation and fluid recirculation (see text). (b) Picture of bubbles rising out of the granular bed entraining particles in their wake (PVC 110P; $h_g = 9$ cm; $h_\ell = 18$ cm; $Q = 0.05$ L/min; $L_c = 13.6$ cm; $e = 2$ mm).

where V_g is the volume of a single grain, φ_s is the solid fraction of the suspension, and U_p is the particle settling velocity. As a reminder, L_s represents the typical width occupied by the suspension, which reaches the lateral boundaries of the cell in all the data that will be discussed in this model, so that $L_s \approx L_c$. The particle sedimentation velocity U_p can be expressed using the relative velocity between a particle and the surrounding suspension, which is often written as [48–50]

$$U_p - U = U_s(1 - \varphi_s)^5. \tag{7}$$

Since the Archimedes number Ar, which corresponds to the particle Reynolds number based on the Stokes velocity $U_s = \Delta\rho g d^2/(18\mu)$, is smaller than 1 (see Table I), the Stokes velocity U_s is the pertinent settling velocity, and the term $(1 - \varphi_s)^5$ corresponds to the correction due to collective effects [51,52]. The velocity U corresponds to the velocity of the suspension, which is the volume average velocity, and takes into account the velocity of the particles U_p and the velocity of the fluid U_c due to the recirculation generated by the rising bubbles:

$$U = \varphi_s U_p + (1 - \varphi_s)U_c. \tag{8}$$

Using mass conservation, the average fluid velocity given by the recirculating flow is $U_c = U_b L_b/(L_s - L_b)$. The particle velocity on the cell sides can therefore be written as $U_p = U_c + U_s(1 - \phi_s)^4$ and leads to an expression for the number of particles settling on the granular bed during dt:

$$dN^+ = \varphi_s \frac{(L_s - L_b)e}{V_g}\left[U_s(1 - \varphi_s)^4 + \frac{U_b L_b}{L_s - L_b}\right]dt. \tag{9}$$

B. Entrainment

Let us denote dN^- the number of particles entrained by the bubbles during the same time interval dt [Fig. 6(a), black zone in the central column]. The entrained particles can come either from the granular bed or from the recirculating suspension. We thus write

$$dN^- = (\chi_s\varphi_s + \chi_b\varphi_b)\frac{L_b e U_p^c dt}{V_g}, \tag{10}$$

where χ_s and χ_b are coefficients representing the fraction of particles entrained from the suspension, χ_s, or the granular bed, χ_b, and U_p^c is the particle velocity in the bubble's wake. The latter can be written, as previously for the particles on the cell sides, as the velocity composition between the fluid, equal to the bubble rising velocity U_b in the central column, and the term due to particle sedimentation:

$$U_p^c - U^c = U_s(1-\varphi_s)^5, \tag{11}$$

in which U^c is the velocity of the suspension in the central region and is given by an average between the velocity of the particle U_p^c and the fluid velocity, equal to the bubble velocity U_b:

$$U^c = \varphi_s U_p^c + (1-\varphi_s)U_b. \tag{12}$$

The combination of the two previous equations leads to

$$U_p^c = U_b - U_s(1-\varphi_s)^4. \tag{13}$$

The number of particles entrained during a time interval dt is therefore

$$dN^- = (\chi_s\varphi_s + \chi_b\varphi_b)\frac{L_b e}{V_g}[U_b - U_s(1-\varphi_s)^4]dt. \tag{14}$$

C. Stationary state

In the stationary state, $dN^+ = dN^-$. We introduce the dimensionless variables $\ell = L_b/L_s$ and $u = U_b/U_s$. Note that the parameter u represents the inverse of a Rouse number defined as the velocity ratio between the entraining, rising fluid and the sedimentation of a single particle. After some algebra, one gets the following relation for φ_s^*, the solid fraction in the suspension in the stationary regime:

$$\varphi_s^* = (\chi_s\varphi_s^* + \chi_b\varphi_b^*)\frac{u-(1-\varphi_s^*)^4}{u+\frac{1-\ell}{\ell}(1-\varphi_s^*)^4}. \tag{15}$$

V. PARTICLE SUSPENSIONS

In this section, we compare the average solid fraction of the suspension inferred from experimental measurements of A^*/A_0, in the stationary regime [Eq. (3)], with the model prediction of its variation upon u, ℓ, and φ_b^* [Eq. (15)]. In Sec. V A, we propose an estimate of the typical bubble size and velocity. χ_s and χ_b are *a priori* unknown and will be discussed in Sec. V B.

A. Typical bubble size and velocity

In confined geometries previous studies have shown that the thickness e_f of the lubrication film between the bubble and the wall is given by $e_f/e \sim \mathrm{Ca}^{2/3}/(1+\mathrm{Ca}^{2/3})$, where $\mathrm{Ca} = \mu U_b/\sigma$ is the capillary number [53,54] and $\sigma \simeq 22$ mN/m is the air/ethanol surface tension at room temperature. In our experiments, a rough estimate of the bubble velocity is $U_b \sim 10$ cm/s, leading to $e_f/e \ll 1$. We can therefore estimate the bubble volume as their apparent surface S, computed from the images, multiplied by the cell gap e. The typical bubble size can then be estimated as its equivalent diameter, $L_b = \sqrt{4S/\pi}$.

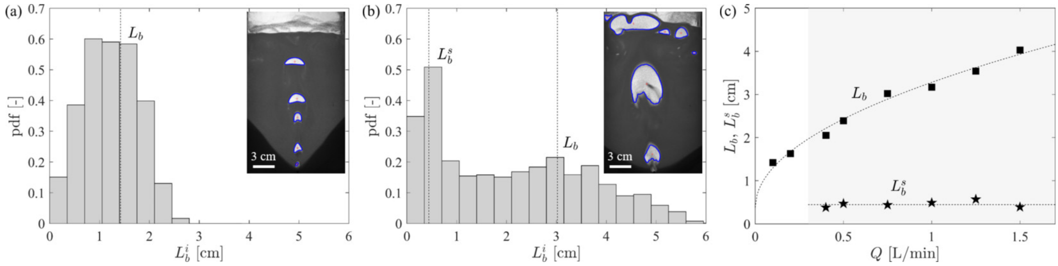

FIG. 7. (a,b) Probability density function of the bubble equivalent diameter (L_b^i indicates the equivalent diameter for bubble i) in the stationary regime. The inset displays a snapshot of the corresponding image sequence with bubble contour (blue line) and center of mass (red cross). (a) At low flow rate ($Q = 0.1$ L/min), the bubble population displays a single characteristic size L_b. (b) At high flow rate ($Q = 0.75$ L/min), small bubbles resulting from bubble fragmentation appear, with a typical size L_b^s. (c) Equivalent bubble diameter as a function of the flow rate Q. For $Q > 0.3$ L/min, we observe two bubble populations [corresponding to the two peaks in (b)]. Small bubbles are roughly constant in size (horizontal dashed line) while large bubbles follow $L_b = 0.38 + 2.9\sqrt{Q}$ (increasing dashed line) (PVC 110P; $L_c = 13.6$ cm; $e = 2$ mm; $h_g = 9.3 \pm 0.5$ cm; $h_\ell = 18 \pm 0.5$ cm).

Figures 7(a) and 7(b) display histograms of the bubble equivalent diameter in the presence of PVC particles, at two different flow rates, in the stationary regime. The picture in the inset of each figure shows an example of the bubble contour detection (in blue). For $Q > 0.3$ L/min, a population of small bubbles appears jointly with the larger bubbles. The maximum of each distribution is picked and reported in Fig. 7(c). The small bubble equivalent diameter, L_b^s, remains roughly constant and of the order of 4.5 mm as a function of the gas flow-rate Q. They are generated by bubble fragmentation and almost always on the sides of the central vertical line above the injection nozzle. Consequently, they do not play any significant role in particle entrainment in the central zone, and will be further ignored. The larger bubble size increases as the square root of the flow-rate, here $L_b = 0.38 + 2.9\sqrt{Q}$ for the PVC 110P. This dependence on $\sqrt{Q}$ does not seem to vary significantly when changing the particles, and is not directly governed by gravity either, as pointed out by previous experiments with PVC particles in tilted cells [55].

The bubble velocity U_b cannot be measured directly in our experiments. Indeed, we capture the stationary state of the suspension over long times, and the acquisition frame rate (1 Hz) is too low to determine the bubble rising speed. From rough observations, we can estimate the bubble velocity between a few and a few tens of centimeters per second. It is of the same order of magnitude as the typical rise time of bubbles in a Hele-Shaw cell filled with water only. Previous works experimentally investigated the velocity of bubbles rising in Hele-Shaw cells and found that, for Reynolds numbers smaller than 10^3, as in our experiments, the bubble velocity can be written as $U_b \sim 0.5\sqrt{gL_b}$ [54,56]. This expression can be interpreted as a simple balance between the buoyancy force and the drag force exerted on the free edges of the bubble, the contribution of the viscous shear stress of the liquid films being negligible [54,56,57].

B. Entrainment mechanism

In Fig. 8, we plot $y = \varphi_s^*/[\frac{u-(1-\varphi_s^*)^4}{u+\frac{1-\ell}{\ell}(1-\varphi_s^*)^4}]$ as a function of φ_s^*. Our experiments have a range of the two parameters ℓ and u of $0.019 < \ell < 0.31$ and $24 < u < 427$, respectively. As predicted by the phenomenological model, for a given type of particles, all data collapse on a linear trend, $\chi_s\varphi_s^* + \chi_b\varphi_b^*$. This result is independent of the height ratio h_ℓ/h_g [Fig. 8(a)] or of the cell width [Fig. 8(c)], as long as $L_s \simeq L_c$ (see Sec. IV). The different coefficients of the linear trend depend on the different batches of grains as indicated by the fit equations provided for all data sets in Fig. 8. The model therefore predicts well, at first order, the behavior of the suspension. Interestingly, for all particles, we find $\chi_s \gg \chi_b$, with χ_s of the order of 90–99 % and χ_b of the order of 2–7 %.

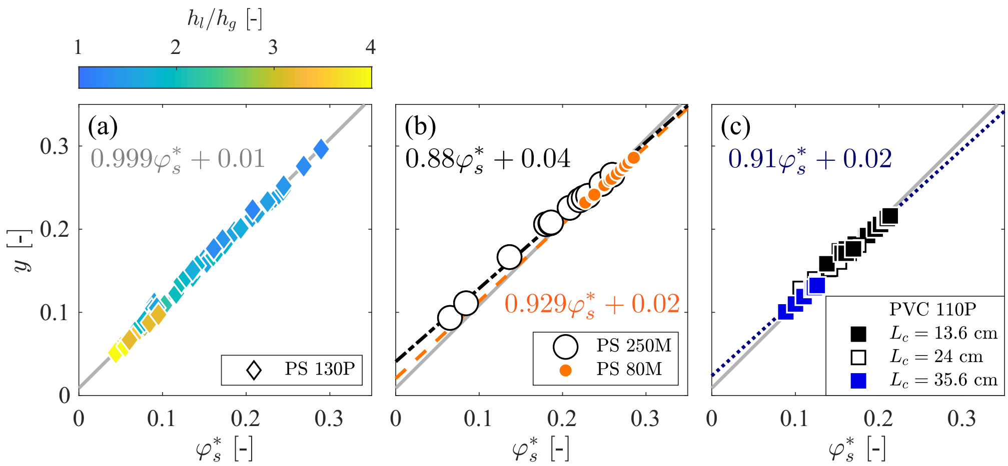

FIG. 8. Parameter y as a function of φ_s^* (see text). Following the prediction of the phenomenological model, $y = \chi_s\varphi_s^* + \chi_b\varphi_b^*$, where χ_s and χ_b depend on the nature of the particles only. (a) PS 130P for different h_ℓ/h_g (cf. color scale) ($L_c = 13.6$ cm, $e = 2$ mm). The solid gray line indicates the linear fit [reported in (b) and (c) for comparison], whose equation is indicated in gray in the figure. (b) PS 250M and PS 80M ($h_g = 9$ cm, $h_\ell = 18$ cm, $L_c = 13.6$ cm, $e = 2$ mm). Dashed black (orange) line: linear fit for the PS 250M (PS 80M) particles. The fit equations are indicated in black (orange) in the figure. (c) PVC 110P ($h_g = 9$ cm, $h_\ell = 16$ cm). All data collapse independently of the cell width L_c (blue dotted line: linear fit, whose equation is indicated in blue) ($e = 2$ mm for $L_c = 13.6$ and 24 cm and $e = 3$ mm for $L_c = 35.6$ cm).

This means that, in the stationary regime, the majority of the particles forming the suspension come from the global recirculation, and not from particles that have settled in the bed and are later extracted and entrained by the bubbles. PS 250M [black dotted line in Fig. 8(b)] and PS 130P [gray thick line in Figs. 8(a) and 8(b)] clearly follow a different linear trend. Several features can explain this difference: the different particle size (see Table I), shape [angular versus spherical; see Figs. 1(b) and 1(c)], or polydispersity (monodisperse PS 250M versus polydisperse PS 130P; see Table I). Figure 8(b) compares two different sizes of the same monodisperse, polystyrene particles, PS 250M, and PS 80M. Although a difference in the linear trend seems to appear, with PS 80M being closer to PS 130P particle trend [gray solid line, Fig. 8(b)], it is difficult at this point to conclude unequivocally. Indeed, the PS 80M particles are easily entrained and sediment very slowly (see Stokes velocity; Table I) and it was impossible, in our experimental conditions, to form suspensions with $\varphi_s^* < 20\%$. Similarly, although the linear trends characterizing the PS 130P and PVC 110P particles appear slightly different [Fig. 8(c)], they cannot be distinguished unambiguously due to the difficulty to span a large range of φ_s^* for PVC 110P. Therefore, within the experimental error bars, we cannot conclude with the present work on the dependence of the parameters (χ_s, χ_b) on the particle sedimentation velocity or polydispersity.

VI. CONCLUSION

In this paper, we have experimentally explored the resuspension of particles of an initially loosely packed immersed granular bed. We have observed that continuous air injection at the bottom of the granular bed leads to a final steady state for different sets of controlling parameters. This final steady state consists of a crater-shaped granular bed and a more or less homogeneous suspension formed by the particles entrained in the above liquid layer by the gas bubbles emerging from the granular bed. The final global characteristics of the suspension are quantified by the spatial-averaged solid fraction, which is computed using the final granular bed volume based on mass conservation. Finally, we have proposed a phenomenological model for the steady state, reflecting the balance between the entrainment of particles by the air bubbles and their settling on the sides of the experimental cell. This model captures with good agreement the main features of the resuspension mechanism using empirical laws for the gas bubble size and velocity. Moreover, we have shown that the suspension is almost "self-sustained," meaning that almost all the particles entrained by the air bubbles come from a global recirculation mechanism and therefore do not go back into the granular bed. Only a few percent of the particles are extracted from the granular bed.

Even if the phenomenological model gives interesting insights into the behavior of suspension generated by gas release, it cannot be predictive. Indeed, it depends strongly on the behavior of the gas bubbles, which depends in particular on the suspension itself. As underlined in [58], bubbles are still a challenge for scientists to understand and/or control their behavior in many complex situations. The effect of the suspension on the dynamics of bubbles is beyond the scope of this paper. It would also be interesting to study not only the global behavior of the suspension but also the local evolution of the solid fraction since the inhomogeneities may be very large. These perspectives shall be the topic of future studies.

ACKNOWLEDGMENTS

We thank D. Bénâtre for insightful discussions. This work was supported by the LABEX iMUST (ANR-10-LABX-0064) of Université de Lyon, within the program "Investissements d'Avenir" (ANR-11-IDEX-0007) operated by the French National Research Agency (ANR). The authors thank two anonymous referees for comments which greatly improved this work.

APPENDIX: STATIONARY STATE

In this Appendix, we show typical snapshots of the final steady states displayed in a similar way as in Fig. 3 for additional sets of external parameters.

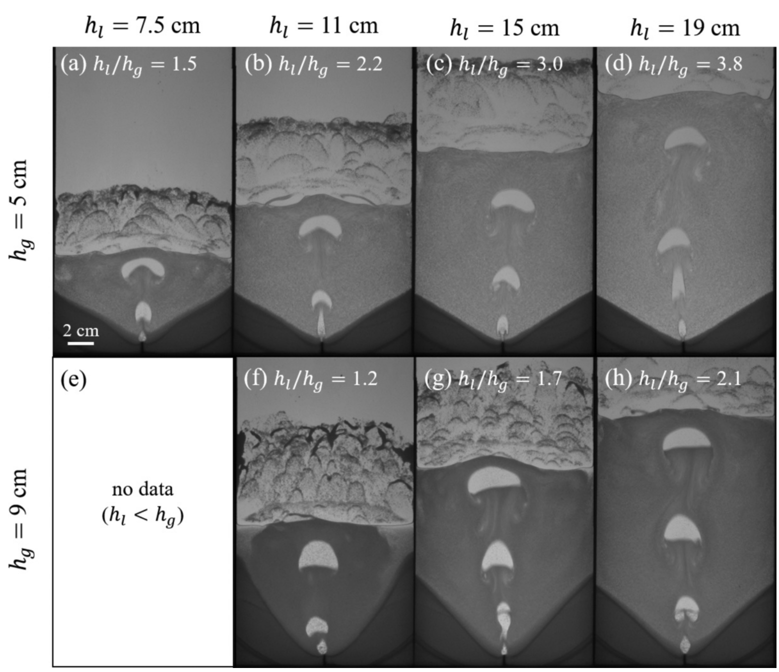

FIG. 9. Snapshots of the experiments in the stationary regime for different granular bed heights h_g and liquid heights h_ℓ (PS 130P; $L_c = 13.6$ cm; $e = 2$ mm; $Q = 200$ mL/min).

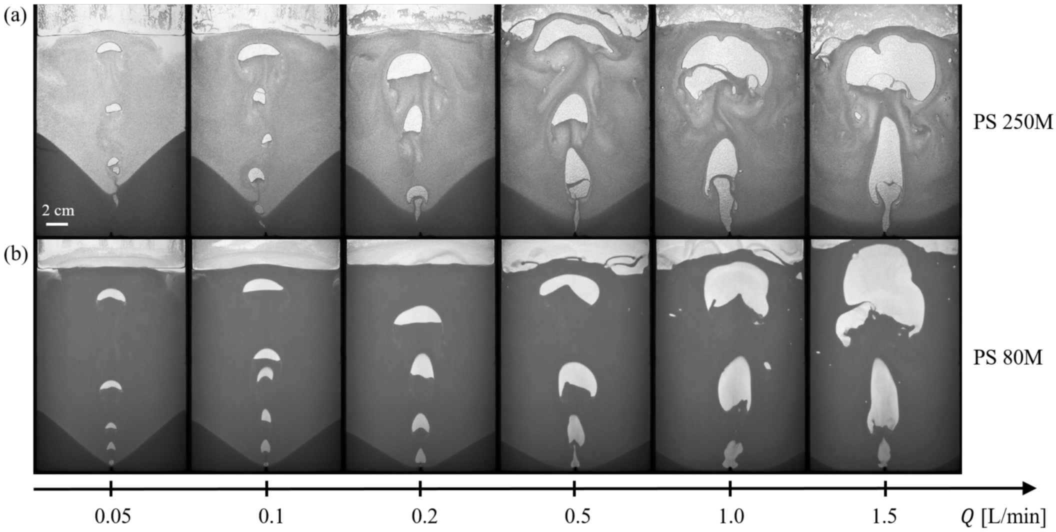

FIG. 10. Snapshots of the experiments in the stationary regime for different values of the flow rate Q and the two different batches of monodisperse particles ($L_c = 13.6$ cm; $e = 2$ mm; $h_g = 9 \pm 0.5$ cm; $h_\ell = 18 \pm 0.5$ cm).

(i) Figure 9 shows the influence of the granular bed height h_g and the liquid height h_ℓ. For each snapshot, the ratio h_ℓ/h_g is given, since it is the important reduced parameter for the computation of the packing fraction of the suspension [see Eq. (3)]. These snapshots show an effect of both parameters on the final granular bed area and the final packing fraction of the suspension, but they do not reveal any clear trend.

(ii) Figure 10 shows the influence of the flow rate Q and the two different batches of monodisperse particles. As expected, the small particles (PS80 M) are more easily put into suspension than larger particles (PS 250M).

[1] T. Dauxois *et al.*, Confronting grand challenges in environmental fluid mechanics, arXiv:1911.09541.

[2] J. Olsen and P. Skjetne, Current understanding of subsea gas release: A review, Can. J. Chem. Eng. **94**, 209 (2016).

[3] A. Judd, M. Hovland, L. Dimitrov, S. Garcia-Gil, and V. Jukes, The geological methane budget at Continental Margins and its influence on climate change, Geofluids **2**, 109 (2002).

[4] H. Svensen, S. Planke, A. Malthe-Sørenssen, B. Jamtveit, R. Myklebust, T. Rasmussen Eidem, and S. S. Rey, Release of methane from a volcanic basin as a mechanism for initial Eocene global warming, Nature (London) **429**, 542 (2004).

[5] L. Naudts, J. Greinert, Y. Artemov, S. Beaubien, C. Borowski, and M. D. Batist, Anomalous sea-floor backscatter patterns in methane venting areas, Dnepr paleo-delta, NW Black Sea, Marine Geol. **251**, 253 (2008).

[6] J. E. Sable, B. F. Houghton, P. Del Carlo, and M. Coltelli, Changing conditions of magma ascent and fragmentation during the Etna 122 BC basaltic Plinian eruption: evidence from clast microtextures, J. Volcanol. Geotherm. Res. **158**, 333 (2006).

[7] J. Oppenheimer, A. Rust, K. Cashman, and B. Sandnes, Gas migration regimes and outgassing in particle-rich suspensions, Front. Phys. **3**, 60 (2015).

[8] K. Cashman, R. Sparks, and J. Blundy, Vertically extensive and unstable magmatic systems: A unified view of igneous processes, Science **355**, eaag3055 (2017).

[9] G. Lawrence, E. Tedford, and R. Pieters, Suspended solids in an end pit lake: Potential mixing mechanisms, Can. J. Civ. Eng. **43**, 211 (2016).
[10] T. Peacock and M. Alford, Is deep-sea mining worth it?, Sci. Am. **318**, 72 (2018).
[11] M. Dudukovic, F. Larachi, and P. Mills, Multiphase catalytic reactors: A perspective on current knowledge and future trends, Catal. Rev. Sci. Eng. **44**, 123 (2002).
[12] N. Rados, Slurry bubble column hydrodynamics, Ph.D. thesis, Sever Institute of Washington Technology, 2003.
[13] K. Pangarkar, T. Schildhauer, J. van Ommen, J. Nijenhuis, F. Kapteijn, and J. Moulijn, Structured packings for multiphase catalytic reactors, Ind. Eng. Chem. Res. **47**, 3720 (2008).
[14] P. Aussillous, J. Chauchat, M. Pailha, M. Médale, and E. Guazzelli, Investigation of the mobile granular layer in bedload transport by laminar shearing flows, J. Fluid Mech. **736**, 594 (2013).
[15] M. Houssais, C. P. Ortiz, D. J. Durian, and D. J. Jerolmack, Rheology of sediment transported by a laminar flow, Phys. Rev. E **94**, 062609 (2016).
[16] S. Badr, G. Gauthier, and P. Gondret, Erosion threshold of a liquid immersed granular bed by an impinging plane liquid jet, Phys. Fluids **26**, 023302 (2014).
[17] B. R. Sutherland and S. Dalziel, Bedload transport by a vertical jet impinging upon sediments, Phys. Fluids **26**, 035103 (2014).
[18] S. Badr, G. Gauthier, and P. Gondret, Crater jet morphology, Phys. Fluids **28**, 033305 (2016).
[19] J. Vessaire, G. Varas, S. Joubaud, R. Volk, M. Bourgoin, and V. Vidal, Stability of a Liquid Jet Impinging on Confined Saturated Sand, Phys. Rev. Lett. **124**, 224502 (2020).
[20] D. Martin and R. Nokes, Crystal settling in a vigorously convecting magma chamber, Nature (London) **332**, 534 (1988).
[21] V. S. Solomatov, P. Olson, and D. J. Stevenson, Entrainment from a bed of particles by thermal convection, Earth Planet. Sci. Lett. **120**, 387 (1993).
[22] G. Lavorel and M. Le Bars, Sedimentation of particles in a vigorously convecting fluid, Phys. Rev. E **80**, 046324 (2009).
[23] C. Morize, E. Herbert, and A. Sauret, Resuspension threshold of a granular bed by localized heating, Phys. Rev. E **96**, 032903 (2017).
[24] E. Herbert, C. Morize, A. Louis-Napoléon, C. Goupil, P. Jop, and Y. D'Angelo, Buoyancy-driven destabilization of an immersed granular bed, J. Fluid Mech. **843**, 778 (2018).
[25] F. E. Loranca-Ramos, J. L. Carrillo-Estrada, and F. Pacheco-Vazquez, Craters and Granular Jets Generated by Underground Cavity Collapse, Phys. Rev. Lett. **115**, 028001 (2015).
[26] M. Houssais, C. Maldarelli, and J. Morris, Soil granular dynamics on-a-chip: fluidization inception under scrutiny, Lab Chip **19**, 1226 (2019).
[27] O. Johnsen, R. Toussaint, K. J. Måløy, and E. G. Flekkøy, Pattern formation during air injection into granular materials confined in a circular Hele-Shaw cell, Phys. Rev. E **74**, 011301 (2006).
[28] C. Chevalier, A. Lindner, and E. Clément, Destabilization of a Saffman-Taylor Fingerlike Pattern in a Granular Suspension, Phys. Rev. Lett. **99**, 174501 (2007).
[29] O. Johnsen, C. Chevalier, A. Lindner, R. Toussaint, E. Clément, K. J. Måløy, E. G. Flekkøy, and J. Schmittbuhl, Decompaction and fluidization of a saturated and confined granular medium by injection of a viscous liquid or gas, Phys. Rev. E **78**, 051302 (2008).
[30] X. Cheng, L. Xu, A. Patterson, H. Jaeger, and S. Nagel, Towards the zero-surface-tension limit in granular fingering instability, Nat. Phys. **4**, 234 (2008).
[31] C. Chevalier, A. Lindner, M. Leroux, and E. Clément, Morphodynamics during air injection into a confined granular suspension, J. Non-Newton. Fluid Mech. **158**, 63 (2009).
[32] B. Sandnes, E. G. Flekkøy, H. A. Knudsen, K. J. Måløy, and H. See, Patterns and flow in frictional fluid dynamics, Nat. Commun. **2**, 288 (2011).
[33] R. Holtzman, M. L. Szulczewski, and R. Juanes, Capillary Fracturing in Granular Media, Phys. Rev. Lett. **108**, 264504 (2012).
[34] N. Hooshyar, J. R. van Ommen, P. J. Hamersma, S. Sundaresan, and R. F. Mudde, Dynamics of Single Rising Bubbles in Neutrally Buoyant Liquid-Solid Suspensions, Phys. Rev. Lett. **110**, 244501 (2013).

[35] C. Madec, B. Collin, J. John Soundar Jerome, and S. Joubaud, Puzzling Bubble Rise Speed Increase in Dense Granular Suspensions, Phys. Rev. Lett. **125**, 078004 (2020).
[36] L. Gostiaux, H. Gayvallet, and J.-C. Géminard, Dynamics of a gas bubble rising through a thin immersed layer of granular material: An experimental study, Granular Matter **4**, 39 (2002).
[37] H. Geistlinger, G. Krauss, D. Lazik, and L. Luckner, Direct gas injection into saturated glass beads: Transition from incoherent to coherent gas flow pattern, Water Resour. Res. **42**, W07403 (2006).
[38] X.-Z. Kong, W. Kinzelbach, and F. Stauffer, Migration of air channels: An instability of air flow in mobile saturated porous media, Chem. Eng. Sci. **64**, 1528 (2009).
[39] G. Varas, V. Vidal, and J.-C. Géminard, Dynamics of crater formations in immersed granular materials, Phys. Rev. E **79**, 021301 (2009).
[40] X.-Z. Kong, W. Kinzelbach, and F. Stauffer, Morphodynamics during air injection into water-saturated movable spherical granulates, Chem. Eng. Sci. **65**, 4652 (2010).
[41] G. Varas, V. Vidal, and J.-C. Géminard, Venting dynamics of an immersed granular layer, Phys. Rev. E **83**, 011302 (2011).
[42] G. Varas, J.-C. Géminard, and V. Vidal, Air invasion in a granular layer immersed in a fluid: Morphology and dynamics, Granular Matter **15**, 801 (2013).
[43] G. Varas, G. Ramos, J.-C. Géminard, and V. Vidal, Flow and fracture in water-saturated, unconstrained granular beds, Front. Phys. **3**, 44 (2015).
[44] B. Andreotti, Y. Forterre, and O. Pouliquen, *Granular Media: Between Fluid and Solid* (Cambridge University Press, Cambridge, 2013).
[45] H. J. H. Brouwers, Particle-size distribution and packing fraction of geometric random packings, Phys. Rev. E **74**, 031309 (2006).
[46] P. Philippe and M. Badiane, Localized fluidization in a granular medium, Phys. Rev. E **87**, 042206 (2013).
[47] G. Gauthier and P. Gondret, Compaction of liquid immersed granular packings by small upward flows, Phys. Rev. Fluids **4**, 074308 (2019).
[48] D. Lhuillier, Migration of rigid particles in non-Brownian viscous suspensions, Phys. Fluids **21**, 023302 (2009).
[49] P. R. Nott, E. Guazzelli, and O. Pouliquen, The suspension balance model revisited, Phys. Fluids **23**, 043304 (2011).
[50] E. Guazzelli and O. Pouliquen, Rheology of dense granular suspensions, J. Fluid Mech. **852**, P1 (2018).
[51] J. Richardson and W. Zaki, The sedimentation of a suspension of uniform spheres under conditions of viscous flow, Chem. Eng. Sci. **3**, 65 (1954).
[52] E. Guazzelli and J.-F. Morris, *A Physical Introduction to Suspension Dynamics*, Cambridge Texts in Applied Mathematics (Cambridge University Press, Cambridge, 2012).
[53] P. Aussillous and D. Quéré, Quick deposition of a fluid on the wall of a tube, Phys. Fluids **12**, 2367 (2000).
[54] M. Roudet, Hydrodynamique et transfert de masse autour d'une bulle confinée entre deux plaques, Ph.D. thesis, Institut National Polytechnique de Toulouse, 2008
[55] V. Vidal, C. Picard, and S. Joubaud, Remontée de bulles dans une suspension dense, in *Comptes-rendus de la 21e Rencontre du Non-Linéaire*, edited by E. Falcon, M. Lefranc, F. Pétrélis, and C.-T. Pham (Non-Linéaire, 2018), Vol. 23, pp. 79–84.
[56] V. Roig, M. Roudet, F. Risso, and A.-M. Billet, Dynamics of a high-Reynolds-number bubble rising within a thin gap, J. Fluid Mech. **707**, 444 (2012).
[57] A. Filella, P. Ern, and V. Roig, Oscillatory motion and wake of a bubble rising in a thin-gap cell, J. Fluid Mech. **778**, 60 (2015).
[58] B. Dollet, P. Marmottant, and V. Garbin, Bubble dynamics in soft and biological matter, Ann. Rev. Fluid Mech. **51**, 331 (2019).